Materials Advances

ROYAL SOCIETY OF CHEMISTRY

PAPER

View Article Online
View Journal

Cite this: DOI: 10.1039/d6ma00434b

Development of dual functional heterostructured g-C_3N_4/CdS nanocomposites for visible light photocatalytic dye degradation and electrochemical hydrogen production

Abida Begum, Kaysar Hamid, Muhammad Zobayer Bin Mukhlish and Md. Tamez Uddin *

This study investigates the synthesis and dual functionality of heterostructured g-C_3N_4/CdS nanocomposites (NCs) for photocatalytic dye degradation and electrochemical hydrogen evolution. The g-C_3N_4/CdS NC was successfully synthesized utilizing a hydrothermal approach. The synthesized NCs were analyzed for their optical, structural, and morphological features using a variety of characterization techniques, such as UV vis DRS, XRD, XPS, TEM, and BET. The photocatalytic performance was evaluated through the decomposition of MB under solar light and visible light. Among the synthesized samples, the 40 wt% g-C_3N_4/CdS NC demonstrated the greatest activity, achieving ~97% degradation of MB within 80 minutes under visible light irradiation. Such improved results stemmed from improved light absorption, increased specific surface area (99.06 m^2 g^{-1}), and diminished recombination of charge carriers. The reduced recombination behavior was further explained based on the band alignment of the heterostructure. Scavenger investigations indicated that conduction band electrons and superoxide radicals were the principal reactive oxidative species facilitating MB degradation. Moreover, electrochemical investigations (LSV, Tafel slope, EIS, and OCP) demonstrated that the heterojunction g-C_3N_4/CdS NCs markedly improved HER activity by enhancing the charge transfer kinetics and reducing the overpotential in comparison to pure CdS and g-C_3N_4. The GC electrode modified with 40 wt% g-C_3N_4/CdS NCs achieved a current density of 10 mA cm^{-2} at an overpotential of only 191 mV, whereas the CdS and C_3N_4-modified electrodes required significantly higher overpotentials of 564 mV and 341 mV, respectively. Exceptional stability and reusability were exhibited by the nanocomposites, maintaining over 91% photocatalytic efficiency after three cycles. Overall, this research underscores the remarkable potential of g-C_3N_4/CdS NCs as efficient, stable, and multifunctional materials for environmental remediation and clean hydrogen production.

Received 28th March 2026,
Accepted 8th June 2026

DOI: 10.1039/d6ma00434b

rsc.li/materials-advances

1. Introduction

Synthetic dyes are widely used in textile, paper, food, leather, printing and cosmetic industries, with the textile sector accounting for nearly two-thirds of global dye consumption.[1,2] Approximately 10–15% of these dyes are released as industrial effluents causing serious environmental concerns.[1] Among them, methylene blue (MB) is a commonly used model pollutant because of its wide industrial applications and frequent presence in wastewater. MB discharge into aquatic environments reduces light penetration, prevents photosynthesis and disturbs the ecological balance.[3] Moreover, MB is highly chemically stable and resistant to biodegradation, and its degradation products can produce toxic and carcinogenic amines, posing serious risks to aquatic organisms and human health.[4] Therefore, effective removal or mineralization of MB before wastewater discharge is essential. Conventional treatment methods such as adsorption, coagulation, oxidation, electrochemical treatment, and biological processes often suffer from high operational cost and secondary sludge generation.[5–14] Hence, there is still a great demand to develop efficient and environment-friendly treatment technologies. Simultaneously, growing fossil fuel consumption has intensified greenhouse gas emissions, climate change, and energy insecurity, driving interest in sustainable energy alternatives.[15] Hydrogen is considered a promising clean fuel because of its high energy density and environmentally friendly combustion products.[16] Electrochemical water splitting has emerged as an

Department of Chemical Engineering and Polymer Science, Shahjalal University of Science and Technology, Sylhet 3114, Bangladesh. E-mail: mtuddin-cep@sust.edu, mtuddin_cep@yahoo.com

attractive hydrogen production route due to its efficiency and scalability.[17,18] However, HER performance strongly depends on electrocatalysts capable of lowering the overpotential and accelerating the charge transfer kinetics. Since the currently widely used electrocatalysts, noble metals such as Pt, are expensive and scarce, developing low-cost, durable, and efficient electrocatalysts is crucial for sustainable hydrogen production.

Over recent years, heterogeneous photocatalysts such as TiO_2, SnO_2, and ZnO have demonstrated promise for degrading organic pollutants.[19–23] However, rapid electron–hole recombination and wide band gaps have limited their industrial applications under solar light irradiation. Therefore, developing efficient visible light active photocatalysts is essential for sustainable photocatalytic applications. Recently, CdS has attracted much attention, mainly because of its narrow band gap ($\sim$2.4 eV) and favorable band-edge positions that enable its strong activity in pollutant degradation, water splitting, and solar conversion.[24–26] However, its practical utility is hampered by quick charge recombination, severe photocorrosion and low electrical conductivity, which consequently raises the overpotential for hydrogen evolution.[27] In addition, graphitic carbon nitride, g-C_3N_4 (g-CN), is appealing due to its facile synthesis, chemical stability, earth abundant nature, and visible light response with a band gap of 2.7–2.8 eV.[28,29] But, pristine g-CN suffers from low intrinsic conductivity, limited active sites, slow charge transfer kinetics, and fast electron–hole recombination, resulting in poor photocatalytic electrochemical performance. To address these issues, forming heterostructures with complementary semiconductors has emerged as an effective strategy.[20,27,30–32] Specifically, g-C_3N_4/CdS heterojunctions can suppress recombination and enhance interfacial charge transfer *via* advantageous band alignment and internal electric fields, consequently enhancing both hydrogen evolution and dye degradation.[33,34] According to the band theory, the conduction band and valence band of g-CN are positioned at more negative potentials relative to those of CdS. Upon contact, the band offsets drive electrons from the CB of g-C_3N_4 to that of CdS, while holes from the VB of CdS to that of g-C_3N_4. This directional flow effectively suppresses the recombination of electron hole pairs and extends the lifetime of charge carriers, leading to increased photocatalytic performance. The accumulation of high energy electrons in the CB of CdS lowers the kinetic barrier for proton reduction, resulting in a drastically reduced HER onset potential.

To better assess the potential of such design strategies, recent advances in dual functional photocatalysts can be critically compared in terms of performance, stability, and synthetic feasibility. Recent literature has demonstrated that heterojunction engineering and elemental doping of graphitic carbon nitride (g-CN) are highly effective strategies for enhancing visible light driven photocatalytic performance by improving charge separation, tuning the band structure, and reducing interfacial resistance.[35–39] For instance, SnS_2 anchored Li-doped g-CN photocatalysts have exhibited excellent activity, achieving up to 99.75% rhodamine B and 89.55% ciprofloxacin degradation within 120 min, which is attributed to efficient heterojunction formation and reduced charge transfer resistance confirmed by electrochemical analyses.[36] Similarly, a type II g-C_3N_4/In_2O_2/SnS_2 ternary heterojunction, fabricated *via* a combined precipitation and heating strategy, delivered outstanding performance with 99.77% Rhodamine B degradation within 100 min and 99.44% ciprofloxacin degradation within 180 min at pH 7, owing to enhanced charge separation, increased donor density, and suppressed recombination.[37] Furthermore, imidazole-assisted carbon doped g-CN (2–5 wt%) has been reported to improve the electronic structure (band gap reduction from 2.47 to 2.37 eV) and achieve up to 92.9% methylene blue degradation under $NaBH_4$-assisted conditions, further confirming the effectiveness of doping-induced electronic modulation in photocatalytic applications.[35] In another study, Devi *et al.* demonstrated that a 100 wt% g-C_3N_4/$NiFe_2O_4$ NC exhibits superior electrocatalytic hydrogen evolution activity with a low over potential (η_{10} = 327 mV) and a reduced Tafel slope (139 mV dec^{-1}), while simultaneously achieving 90.42% Congo red degradation, highlighting efficient heterojunction induced charge transfer.[40] Likewise, $ZnIn_2S_4$ quantum dots coupled with g-C_3N_4 nanosheets formed an efficient S-scheme heterojunction that promoted rapid interfacial charge transfer and enabled concurrent hydrogen evolution and tetracycline degradation under visible irradiation.[41] In spite of the growing interest in dual functional photocatalytic systems, progress in the development of heterostructure g-C_3N_4/CdS NCs for the degradation of organic pollutants and the hydrogen evolution reaction (HER) remains limited. Existing research on g-C_3N_4/CdS NCs primarily focuses on photocatalytic degradation performance for environmental remediation. For instance, studies by Jiang *et al.* and Fang *et al.* have demonstrated high visible light-driven catalytic activity for the mineralization of organic pollutants like methylene blue.[42,43] However, their potential as electrode materials for the electrochemical hydrogen evolution reaction (HER) has been scarcely investigated. Crucial electrochemical parameters such as HER overpotential, Tafel slopes, and charge transfer resistance, are still largely underreported, limiting comprehensive performance evaluation. Furthermore, for g-C_3N_4/CdS NCs reported in the literature, a critical limitation lies in the incomplete understanding of the interfacial charge transfer mechanism, including the precise band alignment, built in electric field formation, and electron–hole separation pathways. As a result, it remains unclear whether the enhanced activity arises from a type II heterojunction, Z-scheme, or alternative charge transfer process, thereby limiting a comprehensive structure–activity correlation and rational design of more efficient photocatalysts. Consequently, detailed investigations linking interfacial electronic structure analysis with photocatalytic degradation and electrochemical HER performance evaluation are essential for the rational design of high performance dual functional heterostructures.

The present work reports hydrothermally synthesized heterostructure g-C_3N_4/CdS NCs designed to promote efficient interfacial contact and improved charge separation. The NC was systematically evaluated for both photocatalytic degradation of MB under visible light and solar light irradiation and the electrochemical hydrogen evolution reaction (HER).

To establish the structure–property relationship, the materials were characterized using XRD, XPS, BET, TEM, and UV Vis spectroscopy, while photocatalytic performance and recyclability were assessed relative to the individual components and commercial TiO_2. The band alignment at the interface of g-CN and CdS in g-C_3N_4/CdS NCs was experimentally determined in order to elucidate the charge transfer mechanism and kinetics. In addition, HER performance was examined by LSV, OCP, and Tafel slope analyses to provide a comprehensive comparison of the dual functional activity.

2. Materials and methods

2.1. Chemicals and reagents

For the preparation of g-CN, CdS, and the g-C_3N_4/CdS photocatalyst, all chemicals were of analytical grade and used as received without any additional purification. Urea, obtained from Sigma Aldrich, was primarily used for synthesizing g-CN nanoparticles. The reagents used for preparing cadmium sulfide (CdS) nanoparticles included sodium sulfide, (Na_2S), thioglycolic acid, ethanol, and cadmium acetate, ($Cd(CH_3COO)_2$. Ethanol was sourced from Sigma Aldrich (Germany), cadmium acetate from Sigma Aldrich (India), sodium sulfide from Merck (India), and thioglycolic acid from Finar. Methylene blue (MB), $C_{16}H_{18}ClN_3S$, used as a model dye was procured from Loba Chemie (India). Deionized water (DI) obtained from an ultrapure system was used throughout the experiment.

2.2. Synthesis of g-C_3N_4/CdS NCs

The g-C_3N_4/CdS NCs were synthesized *via* a hydrothermal method. First, g-CN nanoparticles were prepared by heating urea at 550 °C for 3 hours in a muffle furnace. CdS nanoparticles were synthesized hydrothermally using cadmium acetate ($Cd(CH_3COO)_2$) as a precursor in a Teflon lined stainless steel autoclave at 180 °C. The detailed procedure for the synthesis of g-CN and CdS NPs is described in the supplementary information (SI). To prepare the 40 wt% g-C_3N_4/CdS heterojunction, 1.2 g of CdS and 0.8 g of g-CN were added to 50 mL deionized water under constant stirring for 30 minutes. The well mixed suspension was then transferred into a 50 mL Teflon lined stainless steel autoclave. The autoclave was sealed and placed in an oven at 180 °C for 16 hours. After cooling naturally to room temperature, the product was carefully removed and washed three times with deionized water and absolute ethanol. The collected sediments were dried at 100 °C for 12 hours in an oven. The resulting catalyst, designated as 40 wt% g CNCS, was stored for further use. The same procedure was followed to synthesize g-C_3N_4/CdS catalysts with varying weight percentages of CdS and designated as *x* wt% g-CNCS, where *x* is the mass percentage of g-CN in the NCs.

2.3. Characterization of the NCs

X-ray diffraction (XRD) analysis was carried out using a SMART LAB diffractometer (RIGAKU, Japan) equipped with a Cu anode (Kα radiation) at 45 kV and 200 mA to examine the crystallinity, phase composition, and crystal size of the synthesized nanoparticles. X-ray diffraction patterns were recorded in continuous scan mode, spanning a 2θ range from 10 to 80°. The mean crystalline size (D) was determined using the Scherrer equation: $D = (0.9\lambda)/(\beta_{1/2}\cos\theta_B)$, where λ is the wavelength of Cu Kα (= 1.5405Å), $\beta_{1/2}$ is the full width at half maximum) (FWHM), and θ_B is the diffraction angle. The X-ray photoelectron spectra were recorded using a K Alpha XPS from Thermo Scientific (Thermo Fisher Scientific, UK), employing a monochromatic X-ray source (Kα: 1486.61 eV) produced by an aluminum anode. Using a field emission gun and an accelerating voltage of 200 kV, the Talos F200X G2 TEM apparatus (Thermo Fisher) was utilized to examine the size, shape, morphology, and crystallinity of the produced nanoparticles. A drop of the particle solution was placed onto copper TEM grids that had previously been covered with a carbon coating in order to prepare TEM samples. Low electron doses (70–240 e $Å^{-2}$ for HRTEM and less than 70 e $Å^{-2}$ for SAED) were used to record high resolution transmission electron microscopy (HRTEM) pictures and selected area electron diffraction (SAED) patterns. The textural properties of the nanoparticles were determined *via* nitrogen physisorption at a cryogenic temperature of 77 K conducted using a Micromeritics ASAP 2020 Plus porosimetry analyzer. Prior to characterization, the samples were subjected to a 6 hour degassing procedure at 120 °C under ultrahigh vacuum conditions to remove adsorbed species. The Brunauer–Emmett–Teller approach was utilized to calculate the specific surface areas, whereas the Barrett–Joyner–Halenda protocol was applied to the adsorption branch of the nitrogen isotherms for pore size analysis. The optical band gap energies were determined through UV vis diffuse reflectance spectroscopy performed at room temperature across a wavelength range of 350–800 nm. A PerkinElmer LAMDA 750 UV vis NIR spectrometer was utilized for these measurements, with sintered PTFE employed as the baseline reference standard. A Shimadzu RF 5301PC fluorescence spectrophotometer (Japan) fitted with a 150 W Xenon lamp was used to measure the photoluminescence (PL) characteristics of the G-CN, CdS, and 40% g-CNCS NCs at room temperature.

2.4. Photocatalytic experiments

The photocatalytic activity of commercial TiO_2 (Degussa P25), cadmium sulfide (CdS), graphitic carbon nitride (g-CN) nanoparticles, and the as-synthesized g-CNCS NCs was assessed through the degradation of MB dye in an aqueous solution under visible light irradiation using a LUMATEC Superlite S 04 lamp from Germany. Photocatalytic experiments were carried out in a horizontally positioned Visible Light reactor setup over a 500 mL Pyrex glass beaker. In each experiment, 100 mL of MB dye solution was mixed with 0.05 g of photocatalyst to create a suspension, which was then agitated in the dark for 10 minutes to achieve adsorption desorption equilibrium before being exposed to light. To monitor the MB degradation process, 4 mL aliquots were extracted from the reaction mixture at regular irradiation intervals for subsequent analysis. The concentration of MB was quantified using a UV-Vis spectrophotometer

(LAMDA 750, PerkinElmer, Inc., USA) by measuring the absorbance at 664 nm. Furthermore, to validate the photocatalytic degradation performance of the photocatalysts, two control tests were performed: one using the photocatalyst in the absence of visible light, and another utilizing visible light without the photocatalyst. For comparison, commercial TiO_2 P25 was employed as a reference to monitor the photocatalytic degradation of MB. To explore the degradation efficiency of the prepared nanoparticles, the test experiment was conducted for 180 min under identical conditions. The degradation efficiency was calculated using the subsequent formula (1):

$$\text{Degradation efficiency} = \left(1 - \frac{C}{C_0}\right) \times 100\% \qquad (1)$$

where C denotes the concentration of MB at a specific time t, while C_0 signifies the initial concentration of the MB dye. To validate the photocatalyst's effectiveness in practical, real world conditions, the degradation experiments were also performed under solar light radiation. The experiments were performed under natural sunlight on clear sunny days in May (Bangladesh), where the solar irradiance was approximately 900–1000 W m^{-2}, corresponding closely to standard AM 1.5G solar illumination. The influence of solution pH and photocatalyst dosage on the resulting degradation performance was investigated following the previously described protocol. To ascertain the structural stability and reusability of the catalyst, it was subjected to three consecutive photocatalytic cycles. After each iteration, the material was recovered from the dye suspension *via* centrifugation, cleansed thoroughly with deionized water to remove adsorbed intermediates, and dried at 105 °C before being reintroduced for the next run.

2.5. Electrochemical study

A three electrode cell was employed for all electrochemical measurements, which were conducted on an electrochemical workstation (Corrtest, China). The working electrode consisted of a 0.07 cm^2 glassy carbon disk, while Ag/AgCl and platinum wire served as the reference and counter electrode, respectively. A suite of tests, comprising LSV, OCP, EIS, and Mott–Schottky analysis, was carried out in an aqueous solution of 0.5 mol L^{-1} Na_2SO_4. To prepare the glassy carbon (GC) electrode, the GC was first sonicated for 5 minutes to remove surface contaminants. Subsequently, the electrode was electrochemically cleaned using a cyclic voltammetry (CV) method. The potential was swept from 1.2 V to +0.5 V *vs.* SCE in a 0.5 M sulfuric acid solution, with a scan rate set at 40 mV s^{-1} to achieve steady state conditions. A total of 30 cycles were conducted to ensure thorough cleaning and activation of the electrode surface. A cyclic voltammetry scan was performed to confirm the surface quality of the cleaned glassy carbon electrode. For modification, a catalytic ink was prepared by dispersing 1 mg of photocatalyst powder in a mixture containing 90 μL of ethanol, 90 μL of distilled water, and 10 μL of Nafion solution. This dispersion was subjected to 30 minutes of ultrasonication to ensure a high degree of homogeneity. The GC-g-CN, GC-CdS, and GC-g-CNCS electrodes were then fabricated by drop casting a 6 μL aliquot of the resulting suspension onto the GC surface followed by drying in air at ambient temperature.

3. Results and discussion

3.1. Characterization of the synthesized NCs

The chemical composition and chemical state of the elements of the g-CNCS NCs were evaluated with XPS. The XPS survey spectra of the as-prepared 40 wt% g-CNCS NCs are shown in Fig. 1(A). Fig. 1(A) only shows the emissions from C, N, Cd and S. The absence of additional peaks in the survey scan would suggest that no other significant elements are present, affirming that the g-CNCS NCs primarily consist of carbon, nitrogen, cadmium, and sulfur. The high resolution C 1s spectrum as shown in Fig. 1(B) exhibits two distinct peaks, fitted at binding energies of 285.4 eV and 288.1 eV. The peak at 285.4 eV is attributed to graphitic carbon, indicating strong sp^2 hybridization typical of carbon atoms within the aromatic rings of g-CN. The peak at a higher energy of 288.1 eV may be attributed to the sp^2 hybridization of the carbon atom, formed by two single bonds and one double bond linked to three nitrogen atoms inside the aromatic framework.[44] The high resolution N 1s spectrum (Fig. 1(C)) was deconvoluted into two distinct peaks at 399.20 eV and 399.95 eV. The peak at 399.20 eV is associated with secondary nitrogen (C═N–C), while the peak at 399.95 eV corresponds to tertiary nitrogen (N–$(C)_3$).[45] The Cd 3d spectrum (Fig. 1(D)) exhibits two distinct peaks at binding energies of 405.50 eV and 412.28 eV. These peaks are characteristic of the spin orbit splitting of the Cd 3d core level and are assigned to the Cd $3d_{5/2}$ and Cd $3d_{3/2}$ states, respectively.[46,47] The observed binding energies confirm the presence of cadmium in the Cd^{2+} oxidation state, with the energy separation between the two peaks reflecting the spin orbit coupling of the Cd 3d electrons. Fig. 1(E) shows that the high resolution S 2p spectrum displays two deconvoluted peaks at 161.7 eV and 162.9 eV, attributed to the S $2p_{3/2}$ and S $2p_{1/2}$ spin orbit split states, respectively.[48] These binding energies are indicative of divalent sulfide ions (S^{2-}), confirming their presence in the nanocomposite. The energy separation of 1.2 eV between S $2p_{3/2}$ and S $2p_{1/2}$ is consistent with previous findings.[49,50]

X-ray diffraction (XRD) analysis was conducted to gain valuable insights into the crystalline structure and phase composition of the synthesized nanoparticles. Fig. 2 shows the XRD pattern of the pure CdS, g-C_3N_4, and heterostructure g-C_3N_4/CdS nanocomposites containing different percentages of g-C_3N_4. Fig. 2(a) shows the XRD pattern of g-C_3N_4 where two distinct diffraction peaks at 2θ = 13.11° and 27.35° were observed, which could be attributed to the (100) and (002) plane of g-C_3N_4, respectively.[51,52] The presence of these peaks confirms the formation of graphitic carbon nitride with its characteristic layered structure. The (100) plane reflects the intralayer organization, while the (002) plane highlights the interlayer stacking.[53] The XRD pattern of the hydrothermally synthesized CdS nanoparticles exhibited in Fig. 2(f) possesses the major diffraction peaks at 2θ = 24.6°, 26.4°, 28.4°, 36.5°,

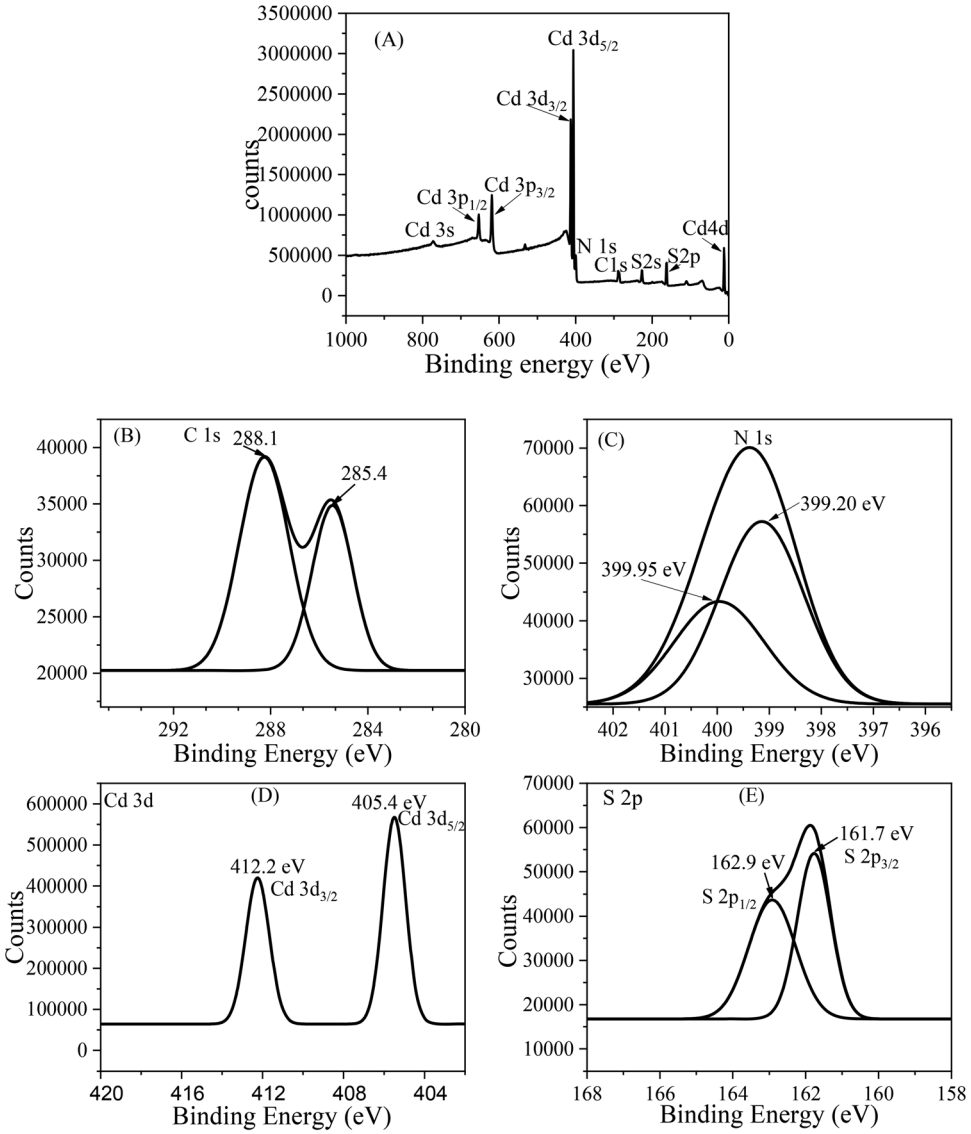

Fig. 1 (A) XPS survey scan spectra and high resolution XPS spectra of (B) C 1s, (C) N 1s, (D) Cd 3d and (E) S 2p energy core levels of 40 wt% g-CNCS NCs.

43.7°, 47.9°, 51.1°, 51.9°, and 52.8° corresponding to the (100), (002), (101), (102), (110), (103), (200), (112), and (201) planes, respectively, of the hexagonal wurtzite structure of CdS and is in good agreement with JCPDS card no. 65-3414.[54] Regardless of the g-C_3N_4 content, the XRD patterns of the heterostructure g-C_3N_4/CdS nanocomposites, shown in Fig. 1(b)–(e), primarily display the diffraction peaks of CdS. The characteristic diffraction peak of g-C_3N_4 at 27.35° is not distinctly visible due to its overlap with the peaks of CdS. The absence of any additional peaks confirms the high purity of both the CdS and g-C_3N_4 nanoparticles in the nanocomposites.

The structural morphology of the as synthesized g-CNCS NCs was examined *via* transmission electron microscopy, with the results displayed in Fig. 3. As shown in the TEM image of the 40 wt% CNCS NCs (Fig. 3(A)), the nanoparticles exhibit a predominantly spherical or near spherical geometry, characterized by an average diameter of 3.25 ± 0.25 nm. High resolution TEM analysis, provided in Fig. 3(B) and (C), was utilized to evaluate the crystalline quality of the composite. The presence of well-defined lattice fringes in the HRTEM images confirms the superior crystallinity of the g-CNCS NCs. This is further supported by the Selected Area Electron Diffraction pattern in Fig. 3(D), where the combination of rings and spots signifies the polycrystalline nature of the nanocrystals.

Analysis of the HRTEM image (Fig. 3(C)) revealed a lattice d spacing of 0.334 nm, which matches the planes of the hexagonal wurtzite phase of CdS. This phase identification is corroborated by the SAED pattern (Fig. 3(D)), where the distinct diffraction rings correspond to planes with the same 0.334 nm spacing. Additionally, a lattice spacing of 0.322 nm was identified, corresponding to the crystallographic plane of graphitic carbon nitride (g-CN). This measurement represents the characteristic interlayer stacking distance within the g CN layered architecture.

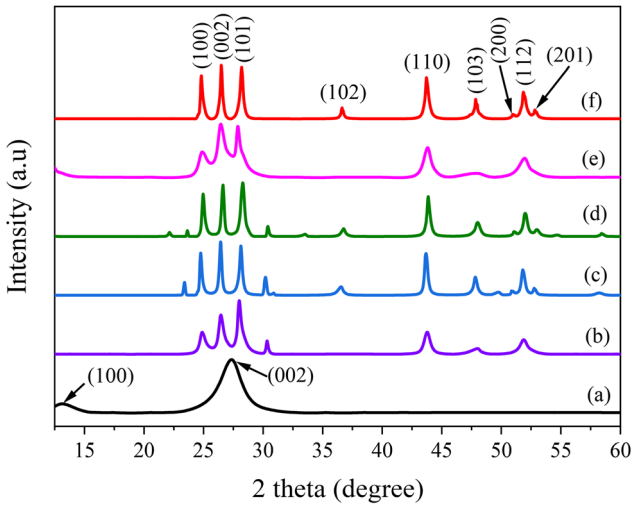

Fig. 2 XRD patterns of (a) g-CN nanoparticles, (b) 20 wt% g-CNCS NCs, (c) 40 wt% g-CNCS NCs, (d) 60 wt% g-CNCS NCs, (e) 70 wt% g-CNCS NCs and (f) CdS nanoparticles.

In order to obtain valuable insights into the potential applications and performance in photocatalytic degradation of the synthesized nanoparticles, textural properties such as surface area, pore size, pore size distribution, pore volume, and pore structure of the synthesized nanoparticles were assessed through N_2 sorption analysis. The N_2 adsorption desorption isotherms and pore size distributions of the pure CdS, g-CN and 40 wt% g-CNCS heterojunction are displayed in Fig. 4. Based on the IUPAC classification, the nitrogen adsorption/desorption isotherms for the 40 wt% g-CNCS NCs demonstrated a type IV behavior, featuring an H2-type hysteresis loop. This behavior is characteristic of mesoporous materials containing complex shaped pores, often described as ink bottle shaped, which arise from the agglomeration of spherical nanoparticles, either consolidated or unconsolidated. The BET surface area, pore volume, and pore diameter of the synthesized nanoparticles are shown in Table 1. The BET surface area (S_{BET}) of CdS and g-CN was found to be 70.38 and 44.05 $m^2\ g^{-1}$, respectively. In contrast, with the incorporation of g-CN with CdS, the BET surface area increased to 99.06 $m^2\ g^{-1}$. The pore size distribution illustrated in Fig. 4(B) indicates that most of the pores in the 40 wt% g-CNCS NCs are located within the mesoporous range with an average pore diameter of 15.26 nm and a pore volume of 0.34 cm^3/g. The increased surface area along with mesoporosity offers additional active sites for light absorption and reaction, thus improving photocatalytic efficiency.

The optical properties of the produced NCs were examined using UV vis diffuse reflectance spectroscopy (DRS) and are shown in Fig. 5. Fig. 5(A) shows that the absorption edges of pure g-CN and CdS were estimated at approximately 440 nm

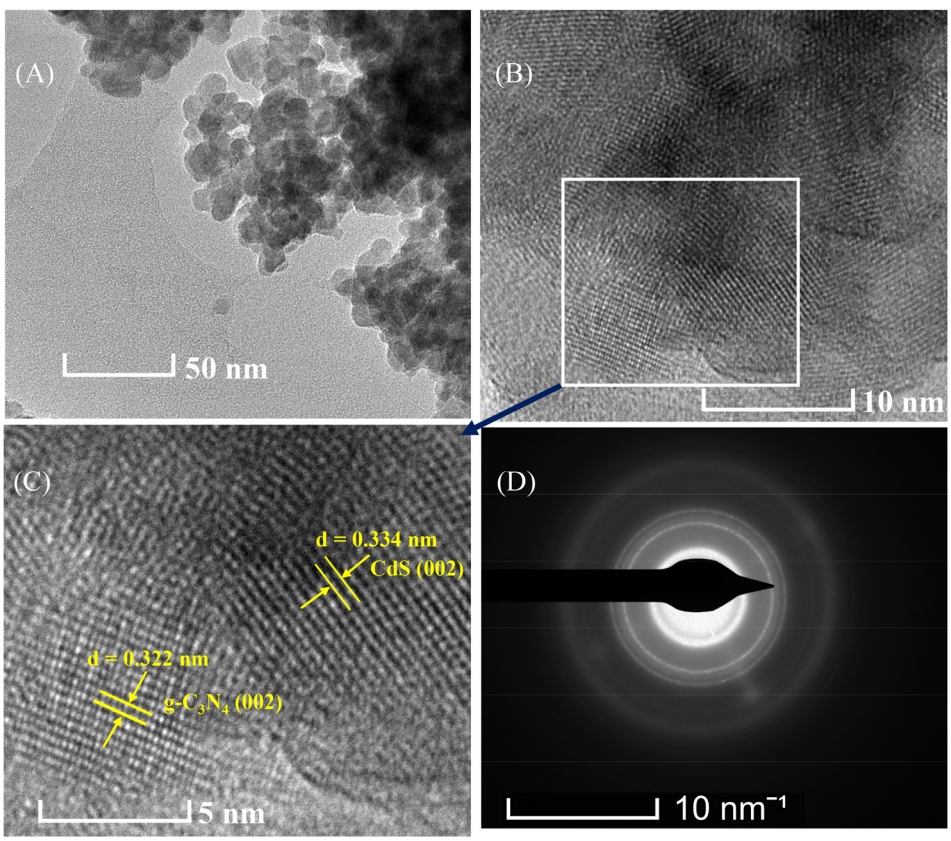

Fig. 3 (A) TEM image, (B) HRTEM image, (C) magnified view of the HRTEM image and (D) SAED pattern of the 40 wt% g-CNCS NCs.

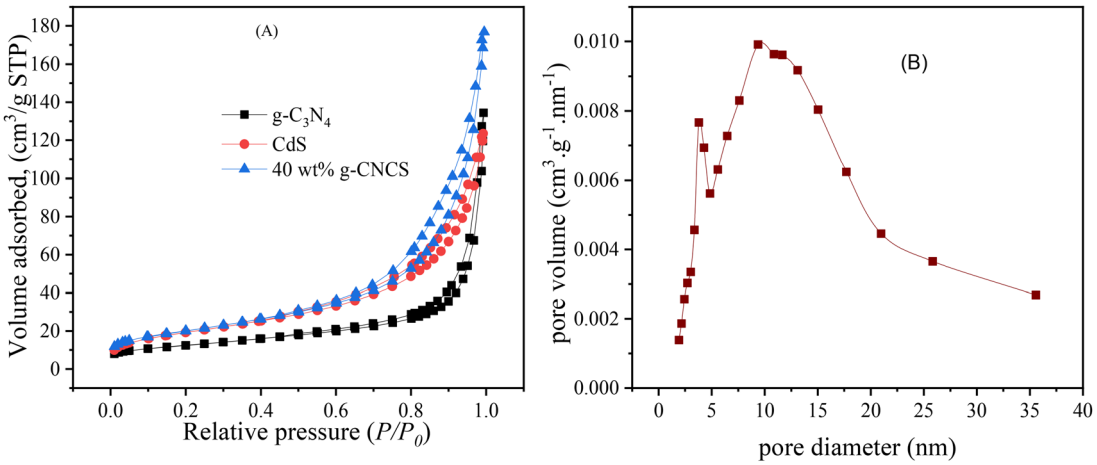

Fig. 4 (A) Nitrogen gas adsorption desorption isotherms of g-CN, CdS and 40 wt% g-CNCS, and (B) pore size distribution of the 40 wt% g-CNCS photocatalyst.

Table 1 Nitrogen sorption porosimetry studies[a] of g-CN, CdS, and g-CNCS nanomaterials

Photocatalyst	S_{BET} ($m^2\ g^{-1}$)	Pore volume ($cm^3\ g^{-1}$)	Average pore size (nm)
g-C_3N_4	44.05	0.17	22.22
CdS	70.38	0.18	11.33
20 wt% g-CNCS	70.30	0.28	16.87
40 wt% g-CNCS	99.06	0.34	15.26
70 wt% g-CNCS	32.47	0.13	17.66

[a] Surface areas were determined by BET, pore diameters by BJH theory (applied to the adsorption branch), and pore volumes by single point analysis.

and 571 nm, respectively. Regardless of the CdS content, the absorption edges of g-CNCS NCs shifted to higher wavelength compared to pure g-CN. The Kubelka–Munk function[55] was used to convert diffuse reflectance data into a form that can be used to determine the band gap energy. The Kubelka–Munk function ($F(R)$) is given by:

$$F(R) = \frac{\alpha}{s} = \frac{(1-R)^2}{2R} \quad (2)$$

where $F(R)$ is the Kubelka–Munk function, R is the reflectance and s is the scattering factor and α is absorption coefficient. $F(R)$ is proportional to the absorption coefficient and is used to replace the absorption coefficient (α) in band gap calculations. Considering an indirect band gap semiconductor, the band gap energy can be determined by using the following equation:

$$[F(R)\cdot h\nu]^{\frac{1}{2}} = B(h\nu - E_g) \quad (3)$$

where $h\nu$ is the photon energy and B is a constant. The band gap energy (E_g) can be determined by plotting $[F(R)\cdot h\nu]^{\frac{1}{2}}$ as a function of photon energy ($h\nu$). The band gap energy of the synthesized photocatalysts was determined by extrapolating the linear region of the $[F(R)\cdot h\nu]^{\frac{1}{2}}$ *vs.* $h\nu$ plot to the x axis

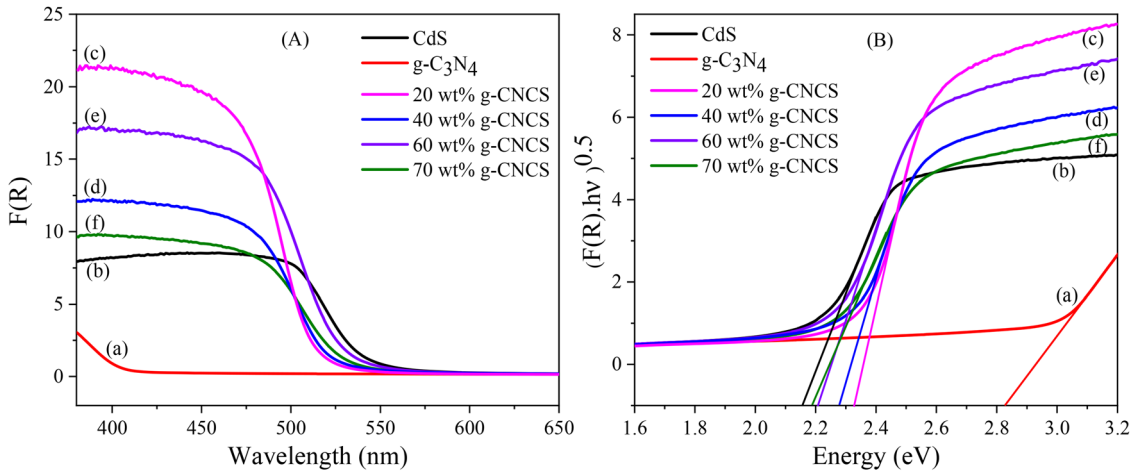

Fig. 5 (A) UV-vis DRS (Kubelka–Munk function) and (B) $(F(R)\ h\nu)^{1/2}$ *vs.* $h\nu$ plot for the synthesized (a) g-C_3N_4, (b) CdS, (c) 20 wt% g-CNCS, (d) 40 wt% g-CNCS, (e) 60 wt% g-CNCS and (f) 70 wt% g-CNCS NCs.

(where $h\nu = E_g$). Fig. 5(B) exhibited the $[F(R) \cdot h\nu]^{\frac{1}{2}}$ *vs.* $h\nu$ plot. The band gap energy of CdS and g-CN was calculated to be about 2.17 eV and 2.71 eV, respectively. The band gap energies of 20 wt% g-CNCS, 40 wt% g-CNCS, 60 wt% g-CNCS, and 70 wt% g-CNCS were determined to be 2.31 eV, 2.27 eV, 2.21 eV and 2.19 eV, respectively.

3.2. Photocatalytic study

The photocatalytic efficiency of the g-CNCS NCs was assessed by degrading the model dye MB under visible light irradiation. Moreover, to confirm the photocatalytic effectiveness of the g-CNCS NCs, control experiments were conducted under visible light without a catalyst and in the dark with the catalyst present. The performance of the synthesized g-CNCS NCs for MB degradation was benchmarked against pristine g-CN, CdS, and commercial TiO_2 (P 25). The preliminary results shown in Fig. 6(A) and (B) demonstrate that the g-CNCS NCs are highly efficient at degrading MB under visible light exposure. During the irradiation process, the characteristic MB absorption peak at 664 nm steadily decreased, suggesting that the dye was almost entirely mineralized or decomposed in the presence of the g-CNCS NCs. This finding was further substantiated by the visible decolorization of the solution over time, as documented in Fig. 6(B). A series of studies were carried out utilizing g-CNCS NC photocatalysts containing differing weight percentages of g-CN to investigate the influence of g-CN NPs in g-CNCS NCs on photocatalytic activity. Fig. 7(A) illustrates the degradation efficiencies of different photocatalysts by a plot of C/C_0 against time (t). Control experiments indicate that MB does not degrade under visible light in the absence of a photocatalyst, and similarly, no degradation occurs when a photocatalyst is present without light irradiation. This indicated that both the photocatalyst and the presence of visible light were essential for the degradation process. Fig. 7(A) also illustrated that the g-CNCS NCs showed enhanced degradation efficiency compared to their individual constituents (pure CdS and pure g-CN), regardless of the g-CN content in the composites.

Specifically, the 40 wt% g-CNCS NCs exhibited the most superior degradation efficiency of all tested photocatalysts. Conversely, commercial P25 remained essentially inactive toward MB under visible light exposure over the observed duration. The degradation efficiency, defined as $(1 - C/C_0) \times 100\%$, for pristine CdS, pristine g-CN, 20 wt% g-CNCS, 40 wt% g-CNCS, 60 wt% g-CNCS and 70 wt% g-CNCS at 80 minutes (selected for comparison, although the reaction was monitored up to 180 minutes) was found to be 47%, 47%, 82%, 97%, 96% and 83%, respectively. Excess g-CN beyond 40 wt% might accumulate on the active surface of CdS, obstructing photocatalytic activation of CdS and decreasing its photocatalytic degradation efficiency.[56] This improved performance can be attributed to enhanced charge separation, leading to more efficient degradation of pollutants.

The photocatalytic degradation reactions can be quantitatively defined using first order kinetics, represented by the equation $\ln(C/C_0) = -kt$, where t represents the reaction time and k denotes the reaction rate constant.[57] Plotting $\ln(C/C_0)$ *versus* t reveals a linear correlation, with the slope representing the reaction rate constant, k. Fig. 6(B) illustrates that the 40 wt% g-CNCS NC photocatalyst exhibits enhanced degradation efficacy, evidenced by a degradation rate constant of 0.107 min, which is 5.94 times higher than that of pure CdS and 10.7 times higher than that of pure g-CN. This improved performance of the g-CNCS NCs resulted from the heterostructure facilitating superior electron hole separation at the interface of the two materials, hence inhibiting charge recombination. A comparative evaluation of the degradation efficiencies achieved by various photocatalytic systems for the removal of organic dyes under visible light is detailed in Table 2. A substantial high rate of MB degradation was demonstrated by the data in Table 2, indicating that the produced g-CNCS NCs have the ability to decompose harmful organic compounds in environmental remediation applications.

The ability of g-CNCS NCs to utilize sunlight efficiently is crucial for environmental remediation, offering an eco-friendly and sustainable solution for the degradation of pollutants.

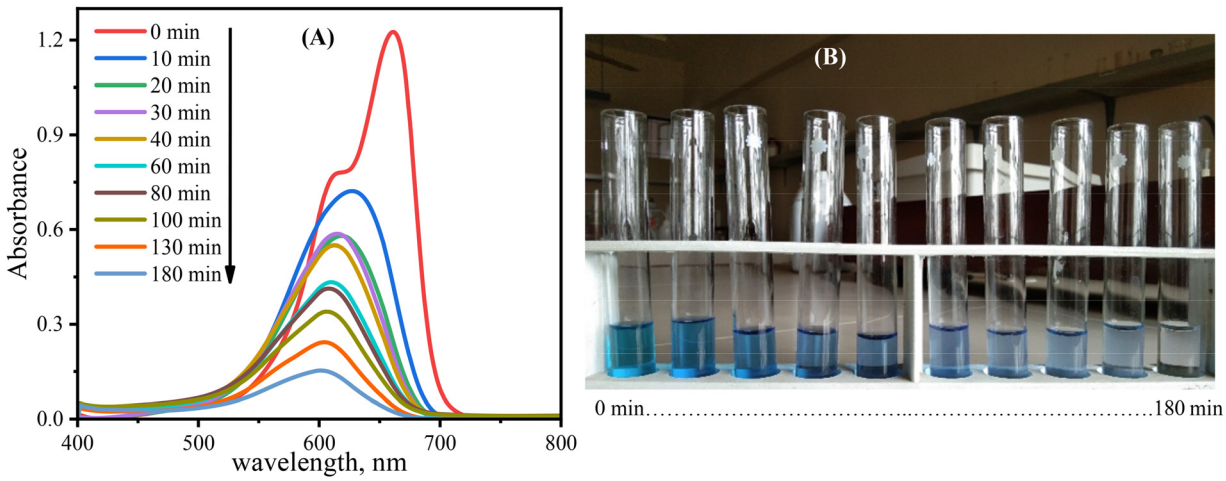

Fig. 6 Change in (A) absorbance and (B) color with time under visible light irradiation in the presence of g-CNCS nanoparticles.

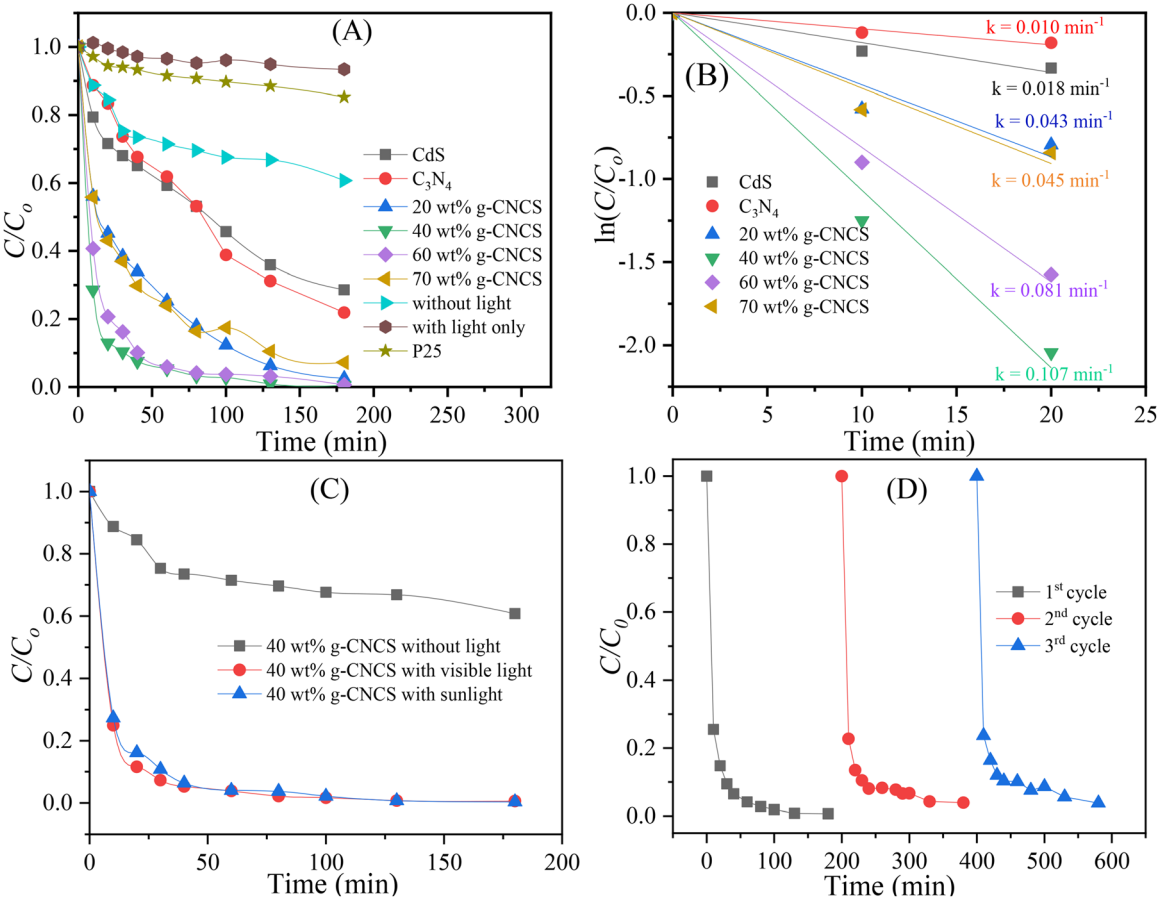

Fig. 7 (A) The photocatalytic MB degradation profile of the as-prepared photocatalysts, (B) MB degradation rate constant of the as-prepared photocatalyst, (C) photocatalytic degradation of MB on 40 wt% g-CNCS NCs under sunlight irradiation and (D) recyclability of 40 wt% g-CNCS NCs for the degradation of MB under visible light. (Initial concentration = 10 mg L^{-1}; solution volume = 100 mL; pH = 7; catalyst dose = 0.5 g L^{-1}).

Table 2 Comparative performance of different photocatalysts in visible light driven degradation of organic dyes

Photocatalyst	Preparation technique	Dye	Catalyst loading	Time (min)	Efficiency (%)	Ref.
CeO_2/CuO	Thermal decomposition	Methylene blue	1 g L^{-1}	210	70	58
ZnO/g-CN	Chemical corrosion	Methyl orange		150	92	59
SnO_2/MoS_2	Sonochemical	Methylene blue	20 mL L^{-1}	120	59	60
N doped g-CN	Calcination	Phenol	1 g L^{-1}	180	70	61
CeO_2/Alumina	Calcination	Methyl orange	0.625 g L^{-1}	90	92	62
CdS/TiO_2	Precipitation	Acid blue	1 g L^{-1}	80	83	63
ZnS/CdS	Microwave	Methylene blue	0.1 g L^{-1}	80	55	64
ZnO/ZnS	Hydrothermal	Methylene blue		80	90	65
C_3N_4/CdS	Hydrothermal	Methylene blue	0.5 g L^{-1}	80	97	Present work

The degradation experiments under solar radiation were performed, as shown in Fig. 7(C), to further validate the photocatalyst's effectiveness in practical, real world conditions. Fig. 7(C) demonstrates that the photocatalytic degradation of MB using 40 wt% g-CNCS NCs in sunlight is very similar to what happens when visible light is used. This test confirmed that the photocatalyst retains its high efficiency under natural sunlight, demonstrating its practical applicability for environmental remediation outside of controlled laboratory settings. This reinforces the potential of the photocatalyst to function effectively in real world scenarios, where sunlight is the primary energy source, offering a sustainable and scalable solution for pollutant degradation and environmental purification. The stability and reusability of the catalyst were assessed through three consecutive uses of the catalyst. Fig. 7(D) demonstrates the photodegradation of MB during these three cycles. After each cycle, the 40 wt% g-CNCS NCs were separated *via* centrifugation, washed with distilled water, and collected in dried powder form. The degradation of a fresh MB solution was then conducted using the catalyst collected from the previous test. After a reaction time of 100 minutes, the photocatalytic efficiencies observed for the three cycles were found to be 98.1%,

93.4%, and 91.4%, respectively. These results indicate that the synthesized photocatalyst exhibits high stability and recyclability, along with effective photoactivity for the degradation of organic contaminants when exposed to visible light. The structural stability of the 40 wt% g-CNCS NCs after the recycling test was further confirmed by XRD analysis. The XRD patterns (Fig. S1 in SI) recorded before and after the photocatalytic cycling experiment exhibited nearly identical diffraction peaks without any noticeable impurity phases or significant peak shifts, indicating that the crystal structure remained stable during repeated photocatalytic reactions. These results demonstrate that the synthesized photocatalyst possesses good reusability and resistance against photocorrosion during repeated photocatalytic cycles.

The pH of the solution plays a vital role in assessing the effectiveness of the degradation process. The surface charge of photocatalysts changes with pH as a result of the ionization of surface hydroxyl groups, influencing the adsorption of dye molecules and the interaction between the dye and the catalyst. The effect of pH on degradation efficiency was exhibited in Fig. 8(A). Fig. 8(A) shows that the degradation efficiency of the 40 wt% g-CNCS catalyst was found to be maximized at pH 7. For the cationic dye MB, a pH higher than 7 enhances its adsorption on the catalyst because of favorable electrostatic interactions with the negatively charged catalyst surface, leading to an increased degradation rate. However, at pH 10, degradation efficiency decreases due to the formation of a thin layer around the catalyst. This layer results from strong electrostatic attraction between the negatively charged catalyst surface and the positively charged MB dye, which hinders light penetration through the porous catalyst and subsequently reduces the rate of the catalytic reaction.[66]

The enhanced degradation efficiency of the CNCS photocatalyst is attributed to the suppressed recombination of photogenerated charge carriers (electrons and holes). This reduction in recombination was validated through photoluminescence spectroscopy. To investigate these recombination rates, PL measurements were conducted on pure CdS, g-CN and 40 wt% CNCS photocatalysts, with the results illustrated in Fig. 8(B). The PL emission peaks provide critical insight into the recombination dynamics: higher peak intensities indicate increased recombination, whereas lower intensities reflect reduced recombination and more efficient charge carrier separation.[67] As shown in Fig. 8(B), the PL emission peak exhibits a slight redshift from 472 nm for pure CdS to 479 nm for the 40 wt% CNCS NCs, signifying strong interactions between the CdS and g-CN components. This result suggests that g-CN acts as an efficient co-catalyst, promoting charge separation and transfer while suppressing charge recombination. The synergistic interaction between CdS and g-CN enables better electron migration, prolongs the carrier lifetime, and enhances the photocatalytic activity of the composite material, making the composite a promising candidate for advanced photocatalytic applications.

3.3. Electrocatalytic HER study of g-CNCS NCs

The electrochemical experiments, including linear sweep voltammetry (LSV), Tafel slope analysis, electrochemical impedance spectroscopy (EIS), and open circuit potential (OCP) for pure CdS, pure g-CN and 40 wt% CNCS NC were systematically analyzed and are depicted in Fig. 9(A)–(E). These analyses were conducted to evaluate and compare their hydrogen evolution reaction (HER) performance and to further validate the behavior of photogenerated charge carrier recombination. The LSV analysis in Fig. 9(A) reveals that the HER onset potential for the CdS and g-CN modified glassy carbon (GC) electrode are 0.38 V and 0.18 V, respectively, whereas the 40 wt% g-CNCS NC modified GC electrode demonstrates a significantly lower onset potential of 0.11 V. The lower onset potential indicates that the CNCS NC modified electrode requires less energy to initiate the HER, demonstrating its superior electrocatalytic activity compared to pure CdS. Additionally, the 40 wt% g-CNCS NC modified GC electrode exhibits a higher reduction current density than the CdS and g-CN modified electrode at a certain potential, signifying a lower hydrogen evolution overpotential and enhanced hydrogen evolution kinetics. At an overpotential of 210 mV, the g-CNCS NC delivers an impressive

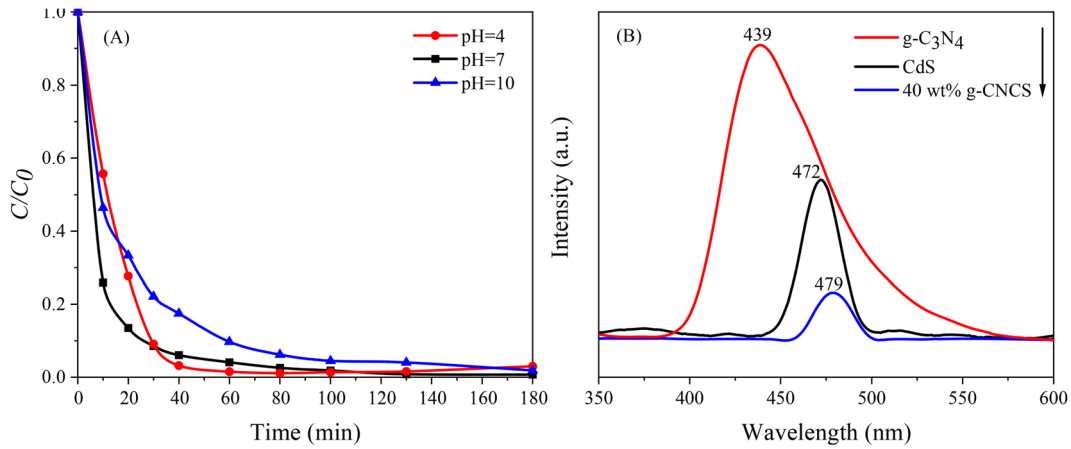

Fig. 8 Effect of pH of MB dye solution on the degradation performance of 40 wt% CNCS NCs and (B) PL emission spectra of the synthesized CdS, g-CN and 40 wt% CNCS photocatalysts.

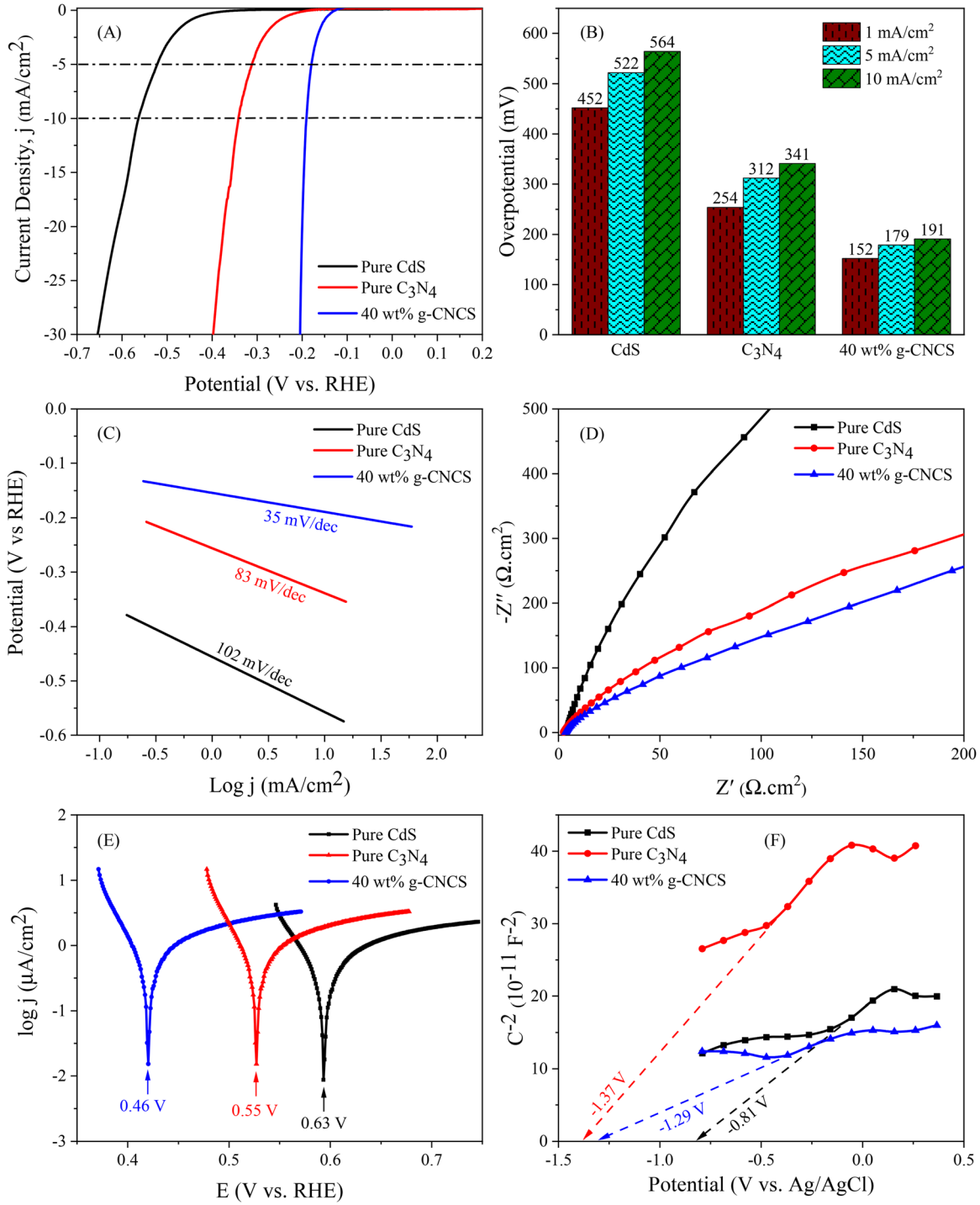

Fig. 9 Electrochemical Behavior Studies. (A) LSV polarization plots toward the HER, (B) comparison of overpotentials at the current densities of 1, 5, and 10 mA cm^{-2}, (C) corresponding Tafel slopes for the HER, (D) EIS (Nyquist plots), (E) OCP plots and (F) Mott Schottky Curves of pure CdS, pure g-CN and 40 wt% g-CNCS NC.

current density of 56.3 mA cm^{-2}, which is approximately 268 times and 703 times higher than that of g-CN and CdS, respectively. This finding highlights the limited HER activity of individual g-CN and CdS materials and the significant enhancement achieved by their combination into a composite. Notably, the GC electrode modified with 40 wt% g-CNCS NC achieves a current density of 10 mA cm^{-2} at an overpotential of only 191 mV, whereas the CdS and g-CN modified electrodes require significantly higher overpotentials of 564 mV and 341 mV, respectively. Fig. 9(B) summarizes the overpotentials required to achieve current densities of 1, 5, and 10 mA cm^{-2}, clearly demonstrating that the g-CNCS NC

modified electrode exhibits the lowest overpotential among the materials tested.

The HER kinetics were further investigated through Tafel slope analysis, a key parameter for assessing catalytic reaction rates. A lower Tafel slope corresponds to a faster catalytic process, which is critical for efficient HER activity. As depicted in Fig. 9(C), the Tafel slope of the g-CNCS NC modified electrode (35 mV dec^{-1}) is remarkably low, compared to 102 mV dec^{-1} for CdS and 83 mV dec^{-1} for g-CN. These results underscore the ability of g-CN incorporation to enhance the electrocatalytic performance for the HER by improving electron transfer and accelerating the reaction kinetics.

The EIS data in Fig. 9(D) further validate the superior HER performance of the g-CNCS NC modified GC electrode. The semicircle diameter observed in the Nyquist plot represents the charge transfer resistance (R_{ct}), a key parameter for evaluating the kinetics of hydrogen ion reduction. A lower semicircle diameter, corresponding to a reduced R_{ct}, indicates enhanced HER kinetics due to improved charge transfer efficiency.[68,69] From the Randle's circuit fitting of the Nyquist plot, the R_{ct} values for the GC electrode modified with pure CdS, pure g-CN and 40 wt% CNCS are calculated to be 18840 kΩ, 1813 Ω and 322 Ω, respectively. The drastic reduction in R_{ct} for the 40 wt% CNCS NC modified GC electrode highlights the enhanced charge transfer efficiency at the electrode electrolyte interface. This reduction in charge transfer resistance demonstrates the improved electron transfer kinetics, which are critical for accelerating the conversion of hydrogen ions (H^+) to molecular hydrogen (H_2). The lower R_{ct} achieved by the g-CNCS NC is indicative of its superior electrocatalytic performance and enhanced HER kinetics.

The OCP measurements in Fig. 9(E) provide additional insights into the enhanced performance of the 40 wt% g-CNCS NC modified GC electrode. The OCP values for the CdS, g-CN and g-CNCS NC modified GC electrodes are recorded as 0.63 V, 0.55 V and 0.46 V, respectively. A more negative OCP value reflects a greater accumulation of negative charges on the electrode surface, thereby creating a favorable reduction environment for the HER.[69] The enhanced reduction environment facilitated by the integration of C_3N_4 into CdS promotes efficient hydrogen ion adsorption on the GCE g-CNCS electrode, further boosting HER activity. The synergistic interplay between g-CN and CdS significantly improves the electrochemical environment, favoring the adsorption and reduction of hydrogen ions.

Collectively, the LSV, OCP, and EIS analyses provide robust evidence that the incorporation of g-CN into CdS significantly enhances HER performance. Also, the lower onset potential and reduced charge transfer resistance of the g-CNCS NCs indicate faster charge transfer and more efficient charge separation, leading to a decreased recombination rate, as corroborated by the PL study.[27] The reduced overpotential, improved kinetics, and enhanced electron transfer highlight the potential of g-CNCS NC materials in advancing sustainable hydrogen production technologies.

3.4. Proposed photocatalytic degradation mechanism

The significant enhancement in the photocatalytic activity of the g-CNCS NCs can be primarily attributed to their improved charge carrier separation efficiency. The efficient separation of photogenerated electron–hole pairs depends strongly on the relative band alignment between the two semiconductor components. A well matched band structure facilitates efficient charge migration across the interface, suppressing charge recombination and thereby enhancing photocatalytic activity. The interfacial band alignment between CdS and g-CN provides a rational explanation for the superior performance of the g-CNCS heterostructure. To elucidate the electronic properties, Mott–Schottky (M–S) analysis was performed to determine the semiconductor type and the conduction band (CB) positions of CdS and g-CN. The corresponding valence band (VB) potentials were subsequently estimated using the relation: $E_{VB} = E_{CB} + E_g$, where E_g denotes the optical band gap energy. The slope of the M–S plot indicates the semiconductor type: a positive slope corresponds to n-type and a negative slope to p-type behavior. The intercept of the extrapolated linear region with the potential axis gives the flat band potential, which approximates the CB potential, assuming a conversion of 1 V = 1 eV. The M–S measurements were conducted over a potential range of −0.8 V to +0.4 V, as illustrated in Fig. 9(F). The resulting M–S plots exhibited positive slopes for pure CdS, pure g-CN, and the 40 wt% CNCS composites, confirming their characteristic n-type semiconductor behavior. The flat band potentials were determined to be −0.81 V for CdS, −1.37 V for g-CN, and −1.29 V for the 40 wt% CNCS composites. The intermediate CB potential of the composite relative to its individual components indicates the successful construction of a heterojunction and strong interfacial electronic coupling, which facilitate efficient charge separation and transfer. Based on the experimentally determined band gap energies of 2.17 eV for CdS and 2.71 eV for g-CN, the corresponding VB potentials were calculated to be 1.36 eV and 1.34 eV, respectively.

Fig. 10 illustrates the band alignment of the g-CNCS heterojunction. The relative band positions suggest that the photocatalytic charge transfer follows a type II heterojunction mechanism. This assignment is reasonable because the CB potential of g-CN is more negative than that of CdS, allowing photogenerated electrons to migrate from the CB of g-CN to the CB of CdS. Meanwhile, the VB potential of CdS is slightly more positive than that of g-CN, enabling holes to transfer from the VB of CdS to the VB of g-CN[70] Therefore, the photogenerated electrons and holes are spatially separated on different components of the composite, which effectively suppresses charge recombination and improves photocatalytic activity.

In contrast, a direct Z scheme mechanism is unlikely for the present g-CNCS system. In a typical Z scheme pathway, electrons in the CB of CdS would recombine with holes in the VB of g-CN. However, the VB potentials of CdS (+1.36 eV) and g-CN (+1.34 eV) are almost identical, resulting in a negligible potential difference. Such a small VB offset cannot provide sufficient thermodynamic or kinetic driving force for selective interfacial electron–hole recombination. Moreover, the lack of a

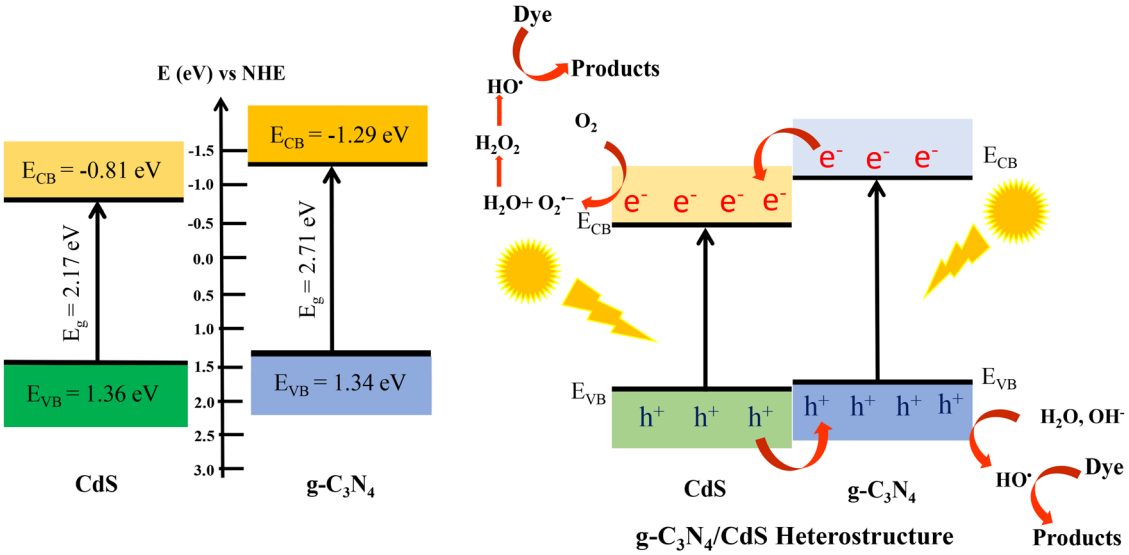

Fig. 10 Energy level alignment and possible electron–hole transfer dynamics in g-CNCS NCs.

significant difference in oxidation potentials weakens the fundamental advantage of a Z scheme system, in which strong redox ability is usually preserved.

Similarly, an S scheme charge transfer mechanism is also unfavorable in this system. The S scheme mechanism generally requires a large difference in Fermi levels and band edge positions to induce strong band bending and establish an internal electric field at the interface. However, in the present CdS/g-CN composite, the limited band edge disparity, especially the nearly identical VB positions and moderate CB offset, is insufficient to generate strong interfacial band bending. Consequently, the charge carrier filtering process characteristic of an S scheme system cannot be effectively realized. Therefore, the experimentally determined band structure is more consistent with a type II heterojunction mechanism rather than a Z scheme or S scheme pathway.

The overall photocatalytic degradation of MB under visible light can thus be explained by the following sequence of reactions.

$$\text{g-}C_3N_4/\text{CdS} + h\nu(\geq E_g) \rightarrow e^- (\text{CdS}) + h^+ (\text{g-}C_3N_4)$$

$$h^+ (\text{g-}C_3N_4) + OH^- \rightarrow OH^\bullet (\text{g-}C_3N_4)$$

$$e^- (\text{CdS}) + O_2 \rightarrow O_2^{\bullet-} (\text{CdS})$$

$$O_2^{\bullet-} (\text{CdS}) + H_2O \rightarrow HO_2^\bullet (\text{CdS}) + OH^-$$

$$HO_2^\bullet (\text{CdS}) + H_2O \rightarrow H_2O_2 (\text{CdS}) + OH^\bullet (\text{CdS})$$

$$H_2O_2 (\text{CdS}) \rightarrow 2OH^\bullet (\text{CdS})$$

$$OH^\bullet (\text{CdS})/OH^\bullet (\text{g-}C_3N_4) + \text{MB} \rightarrow \text{degradation products } (CO_2, H_2O)$$

The holes accumulated in the valence band of g-CN oxidize surface adsorbed water molecules or hydroxyl ions (OH^-) to produce hydroxyl radicals ($OH^\bullet$), whereas the electrons transferred to the conduction band of CdS reduce dissolved oxygen (O_2) to form superoxide radicals ($O_2^\bullet$). These $O_2^{\bullet-}$ species can further react with water to generate additional $OH^\bullet$ radicals. The resulting hydroxyl radicals are strong oxidizing agents capable of degrading organic pollutants such as MB into benign end products including CO_2 and H_2O. Thus, the g-CNCS heterostructure effectively promotes charge separation and redox reactions, leading to superior photocatalytic performance under visible light illumination.

3.5. Validation of the degradation mechanism

To validate the degradation mechanism of the g-CNCS NCs, a series of scavenger experiments were conducted to confirm the involvement of active species in dye degradation. The mechanism centers on the participation of four reactive species: electrons (e), holes (h^+), superoxide anion radicals ($O_2^{\bullet-}$), and hydroxyl radicals ($OH^\bullet$). To selectively inhibit each species, specific scavengers were utilized: EDTA to trap holes, *p* benzoquinone (*p* BQ) to target superoxide anion radicals, $AgNO_3$ to capture conduction band electrons, and isopropanol to scavenge hydroxyl radicals.[27,67,71] The detailed experimental procedure for the scavenger test is described in the SI. The effect of different scavengers on degradation efficiency is exhibited in Fig. 11. As illustrated in Fig. 11(A), the 40 wt% CNCS NCs demonstrated significantly enhanced degradation rates in the presence of EDTA compared to the condition without scavengers. The critical role of EDTA in this system lies in its ability to facilitate charge separation by effectively capturing photogenerated holes from the valence band, thereby reducing electron hole recombination and allowing more free electrons to remain in the conduction band for reduction reactions. This increased availability of conduction band electrons promotes the formation of reactive oxygen species (ROS) such as superoxide anions and hydroxyl radicals, which are highly effective in

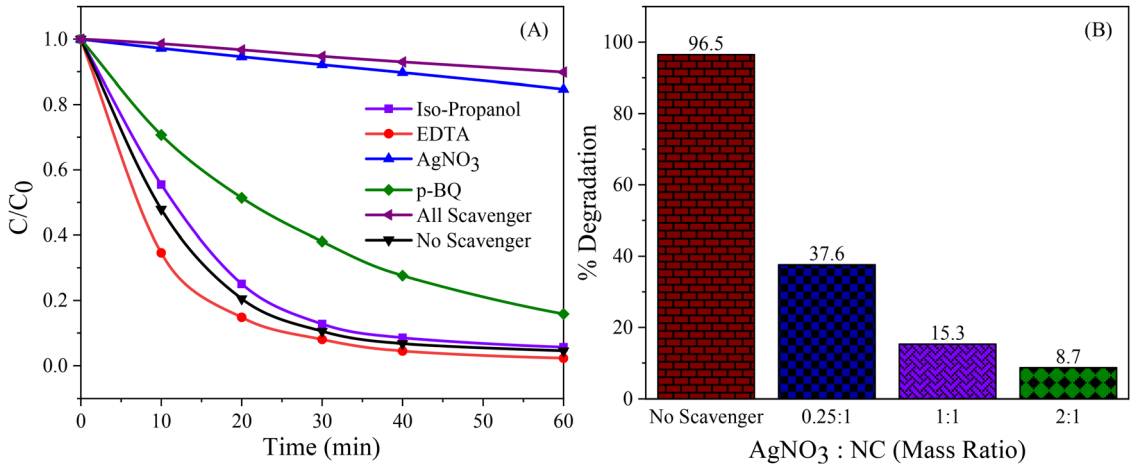

Fig. 11 (A) Effect of different scavengers on photocatalytic degradation efficiency; and (B) effect of scavenger ($AgNO_3$) to NC mass ratio on photocatalytic degradation efficiency.

degrading complex organic pollutants like MB. Moreover, by diverting the degradation pathway away from direct oxidation by holes—often less effective—EDTA encourages ROS mediated reactions that yield a more complete breakdown of pollutants. Additionally, the scavenging action of EDTA helps mitigate photocorrosion, which is the degradation of a photocatalyst's material, often due to the reaction of photogenerated holes with the catalyst itself under light irradiation, leading to deterioration and reduced catalytic activity.[72,73]

In catalysts, reducing photocorrosion enhances stability and longevity in the reaction environment. Overall, using EDTA in the reaction environment results in a more efficient photocatalytic process with improved pollutant degradation and increased catalyst durability. In contrast, introducing $AgNO_3$ almost completely suppresses the MB degradation reaction, highlighting the dependence of ROS generation on conduction band electrons. $AgNO_3$ captures these electrons, which halts ROS formation and thus severely limits MB degradation, reinforcing the importance of conduction band electrons in the photocatalytic mechanism. When *p*-BQ is added, there is a moderate reduction in degradation efficiency, suggesting that superoxide anions are significant contributors to MB breakdown. However, the persistence of some degradation in the presence of *p*-BQ implies that other ROS, such as hydroxyl radicals also participate in the process. Similarly, the use of isopropanol results in a slight decrease in degradation efficiency, indicating that while hydroxyl radicals are involved, they play a secondary role relative to superoxide anions. The moderate degradation observed with *p*-BQ and the slight reduction in degradation with isopropanol, compared to the condition without scavengers, suggests that conduction band electrons may interact directly with MB molecules, providing an alternative degradation pathway. Additionally, some degradation may result from the direct oxidation of MB by photogenerated holes. These findings indicate that the primary degradation pathway for MB in this system involves conduction band electrons generating superoxide anions, with additional contributions from hydroxyl radicals and potential direct electron interactions. This comprehensive analysis of scavenger effects highlights that conduction band electrons and superoxide anions are the dominant species driving MB degradation in the g-CNCS photocatalytic system.

To optimize scavenger concentration for complete suppression of the degradation reaction, experiments were conducted with varying scavenger to NC mass ratios. Fig. 11(B) illustrates the effect of varying $AgNO_3$ to NC ratios on the MB degradation rates. The results show that increasing the $AgNO_3$ to NC ratio reduces the degradation rate. This decrease can be attributed to the higher concentration of $AgNO_3$, acting as an electron scavenger, which introduces more electron trapping sites. These additional trapping sites likely impede the efficient separation and transfer of photogenerated charge carriers, thereby reducing the availability of free electrons required for the photocatalytic degradation of MB.[27] Consequently, the excessive presence of $AgNO_3$ undermines the photocatalytic activity of the system. The optimal suppression ratio was found to be 2 : 1, where 0.1 g of $AgNO_3$ combined with 0.05 g of 40 wt% CNCS photocatalyst effectively minimized the active species generated under irradiation. This specific $AgNO_3$ ratio is sufficient to capture the photogenerated active species, significantly inhibiting the degradation process and confirming $AgNO_3$'s role as an efficient electron scavenger in this photocatalytic system.

4. Conclusion

In this study, the heterostructured g-CNCS NCs were effectively synthesized using a hydrothermal approach and studied for their dual functionality in photocatalytic dye degradation and the hydrogen evolution reaction (HER). The structural, optical, and electrochemical characterization using different techniques demonstrated the successful synthesis of well coupled g-CNCS NCs, which greatly enhanced charge separation,

reduced recombination, and improved visible light absorption. Among the developed photocatalysts, the 40 wt% g-CNCS NCs demonstrated the best photocatalytic activity, achieving approximately 97% MB degradation within 80 minutes and displaying good recyclability across several cycles. The g-CNCS NCs also showed great stability and efficiency when exposed to sunlight, which shows that they can be used in real life as an environmentally benign photocatalyst for cleaning up the environment. Scavenger experiments found that conduction band electrons and superoxide radicals mainly drive the degradation process. Electrochemical tests further indicated that the developed heterojunction reduces charge transfer resistance, lowers the overpotential, and increases the HER kinetics compared to pure CdS and g-CN. This enhancement is attributed to the synergistic electrical contact and favourable band alignment between the two semiconductors. Overall, the results reveal the great potential of g-CNCS NCs as efficient, stable, and multifunctional materials for environmental remediation and clean hydrogen generation. The high performance under both visible light and solar light underscores their practical application and opens a route for the fabrication of scalable dual purpose photocatalysts.

Author contributions

Abida Begum: conceptualization, methodology, formal analysis, investigation, data curation. Kaysar Hamid: writing – original draft, investigation, data curation. Muhammad Zobayer Bin Mukhlish: validation, investigation & visualization. Md. Tamez Uddin: writing – original draft, review & editing, supervision, methodology, funding acquisition, conceptualization.

Conflicts of interest

The authors declare that they have no known competing financial interests or personal relationships that could have appeared to influence the work reported in this paper.

Data availability

The data supporting the findings of this study are available within the article and its supplementary information (SI). Additional data related to this work are available from the corresponding author upon reasonable request.

Supplementary information: contains synthesis details, scavenger studies, and XRD stability analysis of the g-C_3N_4/CdS nanocomposite, supporting the main findings of this work. See DOI: https://doi.org/10.1039/d6ma00434b.

Acknowledgements

The authors express their sincere gratitude to the SUST Research Centre, SUST, Bangladesh, for the financial assistance under Grant No. AS/2023/1/08, which facilitated the experimental work in this study. Appreciation is also extended to the Centre of Excellence at SUST for offering instrumental support for the photocatalyst characterization.

References

1 V. K. Garg, R. Kumar and R. Gupta, *Dye. Pigment.*, 2004, **62**, 1–10.
2 E. Hagan and J. Poulin, *Herit. Sci.*, 2021, **9**, 33.
3 E. Oguz and B. Keskinler, *Colloids Surf., A*, 2005, **268**, 124–130.
4 R. Kishor, D. Purchase, G. D. Saratale, R. G. Saratale, L. F. R. Ferreira, M. Bilal, R. Chandra and R. N. Bharagava, *J. Environ. Chem. Eng.*, 2021, **9**(2), 105012.
5 J. Shu, Z. Wang, Y. Huang, N. Huang, C. Ren and W. Zhang, *J. Alloys Compd.*, 2015, **633**, 338–346.
6 M. Noor, F. Sharmin, M. A. A. Mamun, S. Hasan, M. A. Hakim and M. A. Basith, *J. Alloys Compd.*, 2022, **895**, 162639.
7 M. T. Uddin, Y. Sultana and M. A. Islam, *J. Sci. Res.*, 2016, **8**, 399–411.
8 M. T. Uddin, Y. Nicolas, C. Olivier, L. Servant, T. Toupance, S. Li, A. Klein and W. Jaegermann, *Phys. Chem. Chem. Phys.*, 2015, **17**, 5090–5102.
9 M. Tamez Uddin, M. Rukanuzzaman, M. Maksudur Rahman Khan and M. Akhtarul Islam, *J. Environ. Manage.*, 2009, **90**, 3443–3450.
10 I. Oller, S. Malato and J. A. Sánchez-Pérez, *Sci. Total Environ.*, 2011, **409**(20), 4141–4166.
11 K. Paździor, L. Bilińska and S. Ledakowicz, *Chem. Eng. J.*, 2019, **376**, 120597.
12 M. C. Collivignarelli, A. Abbà, M. Carnevale Miino and S. Damiani, *J. Environ. Manage.*, 2019, **236**, 727–745.
13 Y. Anjaneyulu, N. Sreedhara Chary and D. Samuel Suman Raj, *Rev. Environ. Sci. Biotechnol.*, 2005, **4**, 245–273.
14 J. W. Lee, S. P. Choi, R. Thiruvenkatachari, W. G. Shim and H. Moon, *Dyes Pigm.*, 2006, **69**, 196–203.
15 Afifa, K. Arshad, N. Hussain, M. H. Ashraf and M. Z. Saleem, *Sci. Total Environ.*, 2024, **928**, 172370.
16 Z. Fan, *Highlights Sci. Eng. Technol.*, 2024, **116**, 237–240.
17 M. S. S. Danish, *RSC Sustain.*, 2023, **1**, 2180–2196.
18 B. Ghosh, *African J. Biomed. Res.*, 2025, 1764–1775.
19 M. T. Uddin, Y. Nicolas, C. Olivier, T. Toupance, M. M. Müller, H. J. Kleebe, K. Rachut, J. Ziegler, A. Klein and W. Jaegermann, *J. Phys. Chem. C*, 2013, **117**, 22098–22110.
20 M. T. Uddin, Y. Nicolas, C. Olivier, T. Toupance, L. Servant, M. M. Müller, H. J. Kleebe, J. Ziegler and W. Jaegermann, *Inorg. Chem.*, 2012, **51**, 7764–7773.
21 A. O. Ibhadon and P. Fitzpatrick, *Catalysts*, 2013, **3**(1), 189–218.
22 S. Ahmed, M. G. Rasul, W. N. Martens, R. Brown and M. A. Hashib, *Water, Air, Soil Pollut.*, 2011, **215**, 3–29.
23 S. N. Ahmed and W. Haider, *Nanotechnology*, 2018, **29**, 342001.
24 L. Korala, J. R. Germain, E. Chen, I. R. Pala, D. Li and S. L. Brock, *Inorg. Chem. Front.*, 2017, **4**, 1451–1457.
25 J. A. Nasir, Z. U. Rehman, S. N. A. Shah, A. Khan, I. S. Butler and C. R. A. Catlow, *J. Mater. Chem. A*, 2020, **8**, 20752–20780.

26 H. Anwer, A. Mahmood, J. Lee, K. H. Kim, J. W. Park and A. C. K. Yip, *Nano Res.*, 2019, **12**, 955–972.
27 K. Hamid, M. Z. Bin Mukhlish and M. T. Uddin, *RSC Adv.*, 2024, **14**, 38908–38923.
28 X. Wang, S. Blechert and M. Antonietti, *ACS Catal.*, 2012, **2**(8), 1596–1606.
29 F. Dong, Z. Zhao, T. Xiong, Z. Ni, W. Zhang, Y. Sun and W. K. Ho, *ACS Appl. Mater. Interfaces*, 2013, **5**, 11392–11401.
30 Y. E. Du, X. Niu, X. He, K. Hou, H. Liu and C. Zhang, *Molecules*, 2021, **26**(19), 6031.
31 H. J. Wang, G. G. Yang, S. S. Wu, Z. F. Meng, J. M. Zhang, Y. Cao and Y. P. Zhang, *Sci. Total Environ.*, 2021, **784**, 147221.
32 S. Yuvaraj, A. C. Fernandez, M. Sundararajan, C. S. Dash and P. Sakthivel, *Ceram. Int.*, 2020, **46**, 391–402.
33 F. Opoku, K. K. Govender, C. G. C. E. van Sittert and P. P. Govender, *Adv. Sustainable Syst.*, 2017, **1**, 1700006.
34 J. Liu, *J. Phys. Chem. C*, 2015, **119**, 28417–28423.
35 O. C. Olatunde, D. C. Onwudiwe and S. Makgato, *Results Chem.*, 2025, **17**, 102611.
36 M. Kumari, A. Sharma, N. Kumar, R. K. Sharma, P. R. Makgwane, S. Makgato, M. Tahir and S. Grover, *J. Mol. Struct.*, 2025, **1334**, 141848.
37 M. Kumari, N. Kumar, R. K. Sharma, S. Makgato, M. Tahir, Jogender and A. Kumari, *Mater. Sci. Semicond. Process.*, 2025, **197**, 109658.
38 X. H. Jiang, L. C. Wang, F. Yu, Y. C. Nie, Q. J. Xing, X. Liu, Y. Pei, J. P. Zou and W. L. Dai, *ACS Sustainable Chem. Eng.*, 2018, **6**, 12695–12705.
39 A. Akhundi, A. Zaker Moshfegh, A. Habibi-Yangjeh and M. Sillanpää, *ACS ES&T Eng.*, 2022, **2**(4), 564–585.
40 C. U. Devi, R. Jothilakshmi, R. kabilan, V. Paranthaman, R. Marnadu, V. R. Minnam Reddy, W. K. Kim, I. M. Ashraf and M. Shkir, *J. Mater. Sci.: Mater. Electron.*, 2025, **36**, 2128.
41 J. Zhang, X. Gu, Y. Zhao, K. Zhang, Y. Yan and K. Qi, *Nanomaterials*, 2023, **13**, 305.
42 J. Fang, K. Xie, Q. Kang and Y. Gou, *J. Sci.: Adv. Mater. Devices*, 2022, **7**, 100409.
43 F. Jiang, T. Yan, H. Chen, A. Sun, C. Xu and X. Wang, *Appl. Surf. Sci.*, 2014, **295**, 164–172.
44 J. Zhang, M. Zhang, G. Zhang and X. Wang, *ACS Catal.*, 2012, **2**, 940–948.
45 A. Kumar, P. Kumar, A. K. Pathak, A. N. Chokkapu and S. L. Jain, *ChemistrySelect*, 2017, **2**, 3437–3443.
46 F. Wu, X. Zhang, L. Wang, G. Li, J. Huang, A. Song, A. Meng and Z. Li, *Small*, 2024, **20**, 2309439.
47 J. F. Moulder, W. F. Stickle, P. E. Sobol and K. D. Bomben, *Handbook of X-ray photoelectron spectroscopy: a reference book of standard spectra for identification and interpretation of XPS data*, 1992.
48 L. Wang, M. Meng, R. Zheng, X. Li and H. Yuan, *Nanomaterials*, 2022, **12**, 3190.
49 M. Sabarinathan, S. Harish, J. Archana, M. Navaneethan, H. Ikeda and Y. Hayakawa, *RSC Adv.*, 2017, **7**, 24754–24763.
50 D. Ma, Q. Lu, E. Guo, F. Tao and M. Wei, *ChemistrySelect*, 2021, **6**, 2561–2568.
51 M. Lu, Z. Pei, S. Weng, W. Feng, Z. Fang, Z. Zheng, M. Huang and P. Liu, *Phys. Chem. Chem. Phys.*, 2014, **16**, 21280–21288.
52 S. Shenoy, K. Tarafder and K. Sridharan, *Phys. B*, 2020, **595**, 412367.
53 W. Wei, J. Luo, S. Liu, Y. Zhou and J. Ma, *J. Solid State Chem.*, 2022, **312**, 123160.
54 Z. Yan, Z. Sun, X. Liu, H. Jia and P. Du, *Nanoscale*, 2016, **8**, 4748–4756.
55 V. Džimbeg-malčić, Ž. Barbarić-mikočević and K. Itrić, *Tech. Gaz.*, 2011, **18**, 117–124.
56 H. Yang, K. Zhang, R. Shi and A. Tang, *J. Am. Ceram. Soc.*, 2007, **90**, 1370–1374.
57 X. Liu, J. Li and W. Yao, *ACS Omega*, 2020, **5**, 27463–27469.
58 R. Saravanan, S. Joicy, V. K. Gupta, V. Narayanan and A. Stephen, *Mater. Sci. Eng., C*, 2013, **33**, 4725–4731.
59 Y. Zhang, S. M. Zhao, Q. W. Su and J. L. Xu, *Rare Met.*, 2021, **40**, 1–9.
60 A. Rani, K. Singh, A. S. Patel, A. Chakraborti, S. Kumar, K. Ghosh and P. Sharma, *Chem. Phys. Lett.*, 2020, **738**, 2019–2020.
61 D. Zhu and Q. Zhou, *Appl. Catal., B*, 2021, **281**, 119474.
62 P. Latha, K. Prakash and S. Karuthapandian, *Adv. Powder Technol.*, 2017, **28**, 2903–2913.
63 N. Qutub, P. Singh, S. Sabir, S. Sagadevan and W. C. Oh, *Sci. Rep.*, 2022, **12**, 1–18.
64 N. Soltani, E. Saion, W. M. M. Yunus, M. Erfani, M. Navasery, G. Bahmanrokh and K. Rezaee, *Appl. Surf. Sci.*, 2014, **290**, 440–447.
65 L. Yang, Z. Zhao, H. Wang, J. Dong, L. Wang, Q. Zhou, X. Wan, R. Zhao and Z. Cai, *J. Dispersion Sci. Technol.*, 2020, **41**, 2152–2158.
66 M. T. Uddin, PhD thesis, Institute of Molecural Science, University of Bordeaux 1, France, 2013.
67 A. Trenczek-Zajac, M. Synowiec, K. Zakrzewska, K. Zazakowny, K. Kowalski, A. Dziedzic and M. Radecka, *ACS Appl. Mater. Interfaces*, 2022, **14**, 38255–38269.
68 Y. Sun, B. Wang, X. Liu, L. Gao and W. Shangguan, *Catalysts*, 2023, **13**, 1149.
69 M. N. Islam, Z. M. Moushumy, M. R. Islam, M. I. Hossain, M. A. Rahman, M. Rahaman, A. Aldalbahi, M. T. Uddin, N. R. Singha and M. A. Hasnat, *Electrochim. Acta*, 2024, **507**, 145114.
70 M. Yan, Y. Ma, H. Zhang, B. Ye and X. Dong, *J. Phys. Chem. Solids*, 2018, **116**, 50–57.
71 X. Zheng, J. Yuan, J. Shen, J. Liang, J. Che, B. Tang, G. He and H. Chen, *J. Mater. Sci.: Mater. Electron.*, 2019, **30**, 5986–5994.
72 B. Weng, M. Y. Qi, C. Han, Z. R. Tang and Y. J. Xu, *ACS Catal.*, 2019, **9**(5), 4642–4687.
73 J. B. Islam, M. Furukawa, I. Tateishi, S. Kawakami, H. Katsumata and S. Kaneco, *SN Appl. Sci.*, 2019, **1**, 1240.